Structural Wind Analysis of The High-Rise Building 1180 Peachtree Using The Eurocode Standard and CFD Simulations

Guillermo Barraza, Bassel Saridar, Mahmoud Zidan*

Abstract

This paper reports a structural wind analysis performed on the building 1180 Peachtree located in Atlanta, USA, by means of analytical calculations, using the Eurocode1, and CFD simulations, using Kratos. A wind profile is formulated based on real data using Gumbel's method, and the most critical cases are studied. The results of the Eurocode1-based calculations of the aeroelastic static and dynamic responses and the vortex shedding phenomenon are presented, as well as the setup for the CFD simulations and a comparison of the results. Moreover, the impact of the building's geometry on the pedestrian comfort is briefly studied. Finally, the results of the analytical calculations and the CFD simulations are compared.

Keywords: Computational Wind Engineering, Computational Fluid Dynamics, Vortex Shedding

1 Introduction

High rise buildings are more susceptible to wind loads due to their prominent heights. Thus, design of high-rise buildings against wind loads is always one of the biggest challenges engineers face.

A proper high-rise building design should satisfy both ultimate and serviceability limit state conditions against vertical and lateral loads [1]. To ensure a properly designed building, wind standards serve as a primary design tool at early stage of design, followed (in case of having access to them) by more sophisticated testing methods such as Wind Tunnel tests or Computational Fluid Dynamics simulations (CFD).

The application of CFD in wind engineering, called computational wind engineering (CWE), has gradually become a popular tool for engineers and has been widely used for the prediction of wind pressures and wind forces on various buildings and structures [2]. Despite its widespread use, the general assessment of the approach for quantitative and even qualitative predictions is expressed as lack of confidence, being the availability of several physical and numerical parameters, which can be tweaked freely by the user, the main objection. Thus, several comparative studies have been conducted in the last years to assess the influence of different parameters on the numerical method's solution [3, 4]. However, no generally accepted recommendations on the selection of these parameters have yet been blindly accepted to increase the confidence in the use of CFD.

Regardless of the aforementioned statements, several initiatives to set best practice guidelines on the field and creation of new codes are being developed. One of these codes, which was used throughout the span of the project, is Kratos Multi-physics [5]; a framework for building multi-disciplinary finite element programs.

This report brings into focus the aeroelastic behaviour of the 1180 Peachtree, a $\tilde{2}00$ m tall building located in Atlanta, Georgia, United States. In this case study, we compare the analytical wind load calculations based on the *Eurocode* and the numerical results obtained with Kratos.

---
* *MSc students Computational Mechanics, Technical University of Munich*
Supervised by Máté Péntek and PD Dr.-Ing. habil. Roland Wüchner

1.1 1180 Peachtree's general information

1180 Peachtree (Figure 1 [6]) is one of skyscrapes of Atlanta, Georgia, United States, rising 200m above ground in 41-stories. It is commonly known as the Symphony Tower, or "Batman" tower due to its relatively large glass fins on the top. The building includes office and retail space in its 351,616 square meter of floor area as well as a 1,200 space parking deck. The architectural design was established by the renowned firm Pickard Chilton, and was completed in 2006 [7], where mainly the material used for construction is concrete. This building is marked on the skyline by two sweeping glass fins extending upwards from the north and south walls. These fins are illuminated from inside at night for a dramatic skyline presence, giving what is considered to be a "Gothic" feel.

Figure 1: 1180 Peachtree, Georgia, USA

2 Data Collection and Process

The three dimensional model of 1180 Peachtree has been collected from [8]. The simplifications done on the collected model are discussed later in section 4.2. On the other hand, the wind data was aimed to be collected as the yearly maxima for 30 years, but due to the government shutdown in the USA [9] the full data from the National Oceanic and Atmospheric Administration website [10] could not be accessed since the website was closed. As a remedy, daily maxima for eight years was used, which is shown in Figure 2. However, after the CFD simulations were already done and the government shutdown had ended, both the 30 years yearly maxima and the eight years daily maxima have developed nearly the same wind velocity profile.
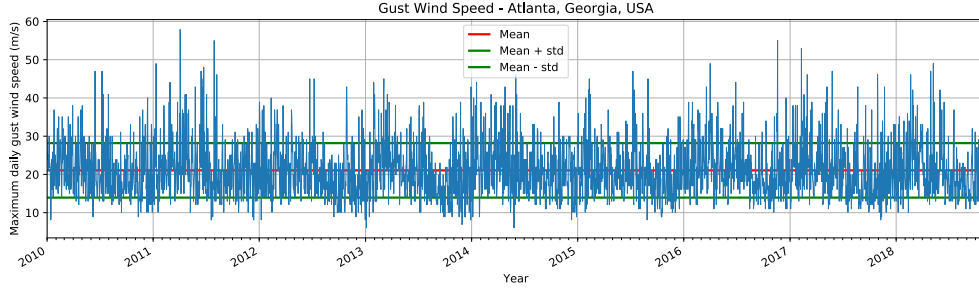
Figure 2: Daily fastest 5 seconds wind speed for eight years

2.1 Extreme Wind Velocity Prediction

Using the obtained data to determine the extreme wind velocity with a return period of 50 years, three methods are used, namely, Gumbel's method, Gringorten's method, and the method of moments. A cumulative probability distribution function,

$$F_u(U) = e^{-e^{-\frac{U-u}{a}}}, \tag{1}$$

is considered. First, Gumbel's method sorts all the wind velocity data points in an ascending manner, and gives them a rank as 1, 2, ..., N, where rank 1 is the smallest wind velocity value and N is the highest. Then, each data point i is given a probability of non-exceedance $p_i = \frac{\text{rank}_i}{N+1}$. Next, a reduced variate, y, is formed such that $y_i = -\ln\left[-\ln\left(p_i\right)\right]$. Finally, a straight line is fitted such that the x-axis is the reduced variate and the y-axis is the gust wind velocity. This linear fitting is depicted in Figure 3.
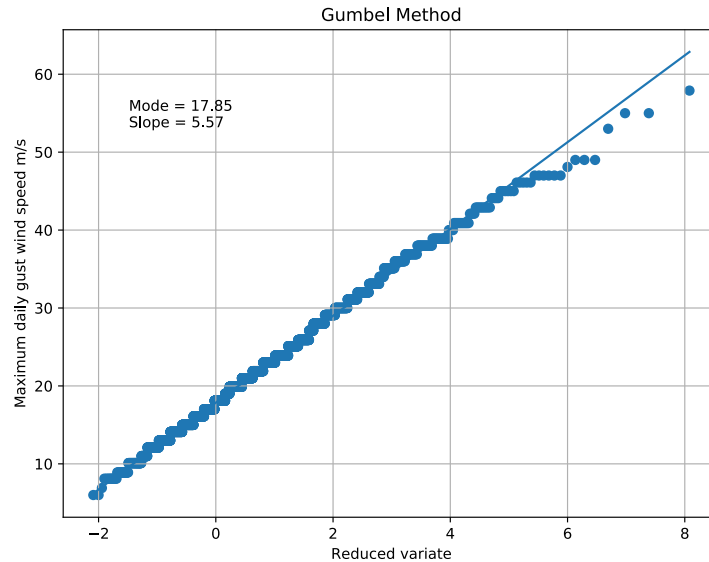

Figure 3: Gumbel's method

The return period extreme velocity is finally obtained as the following equation:

$$U_R = u + a \cdot \left\{ -\ln\left[-\ln\left(\frac{1}{R}\right)\right]\right\}, \tag{2}$$

3

where R is the return period, and u and a are the mode and the slope of the linear fitting, respectively. Gringorten's method, however, differs only in the formula of the probability of non-exceedance, where it is calculated as $p_i = \frac{\text{rank}_i - 0.44}{N + 0.12}$. The method of moments , on the other hand, directly estimates the mode and the slope as $u = \mu - 0.5772a$, $a = \left(\frac{\sqrt{6}}{\pi}\sigma\right)$, where μ is the mean and σ is the standard deviation of the wind data. The return period extreme velocity for the aforementioned two method is calculated as well using (2). Due to the fact that the number of data points is sufficiently large, the three methods yield similar results, which is depicted in Figure 4.
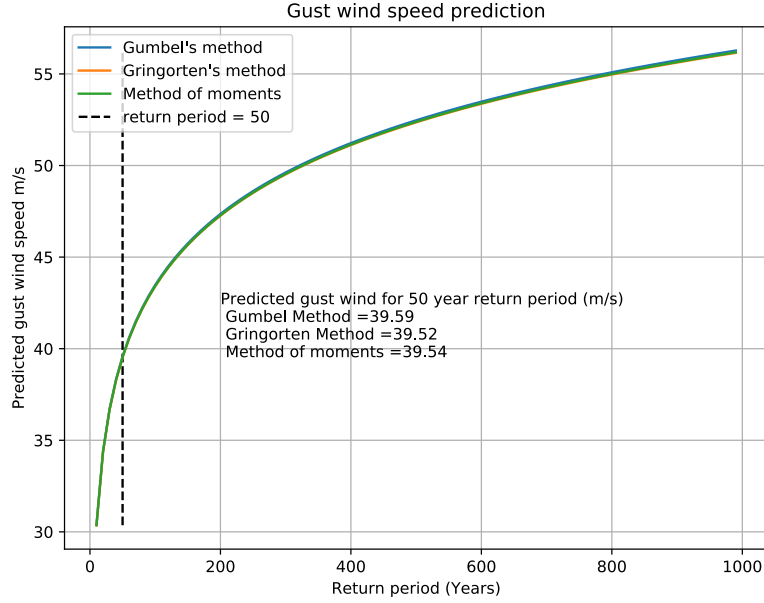

Figure 4: Extreme wind velocity prediction

The maximum wind gust velocity used throughout this work with a return period of 50 years is $U_{50} \approx$ 39.59 m/s according to Gumbel's method.

2.2   Wind Velocity Profile

The wind velocity profile is developed according to Eurocode with an assumption of a category IV terrain [11], which is:

$$
\begin{aligned}
u_{mean}(z) &= 0.56 \cdot v_b \cdot \left(\frac{z}{10}\right)^{0.3}, \\
u_{gust}(z) &= 1.05 \cdot v_b \cdot \left(\frac{z}{10}\right)^{0.2},
\end{aligned}
\tag{3}
$$

where $v_b = U_{50}/1.4$ is an approximate conversion from gust wind speed to mean wind speed, and z is the height of the building starting from zero at the base. The velocity profile is shown in figure 12. It is also worth to mention that the assumption of terrain category IV, which states *"Areas in which at least 15% of the surface is covered with buildings and their average height exceeds 15 m"* [11] is based on the fact that the building is surrounded by high-rise buildings, which is shown in Figure 5.
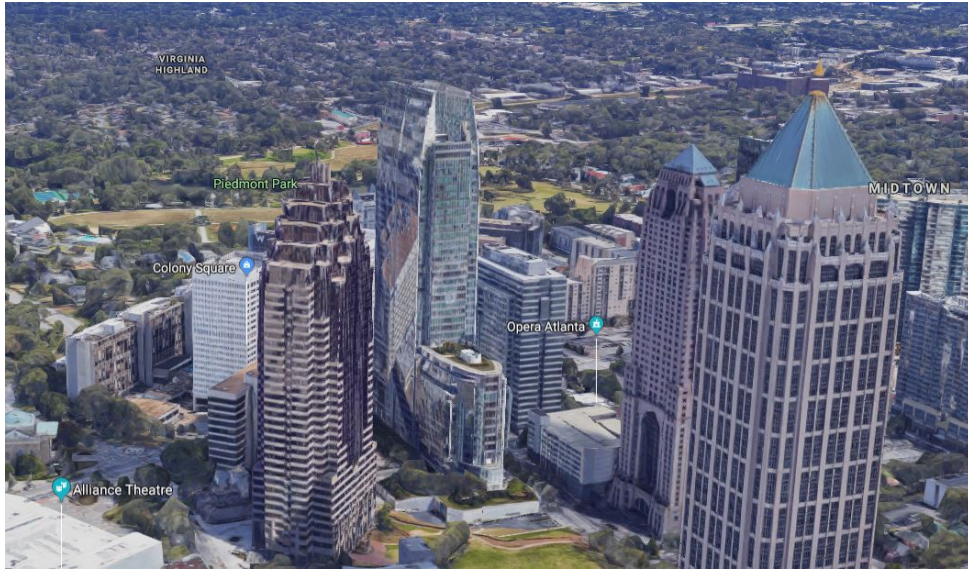
Figure 5: Building's surroundings [Google maps]

2.3 Wind Direction

The dominant wind direction can be determined using the wind rose of the region, depicted in Figure 6 [10]. One can notice that the most frequent wind direction with the high velocities is the north west. However, in this project, it is chosen to simulate the most critical cases were the building has the most surface area across wind direction, leading to the definition of a *first* and a *second configuration* that are carried out throughout this report. These configurations are shown later in Figure 12.
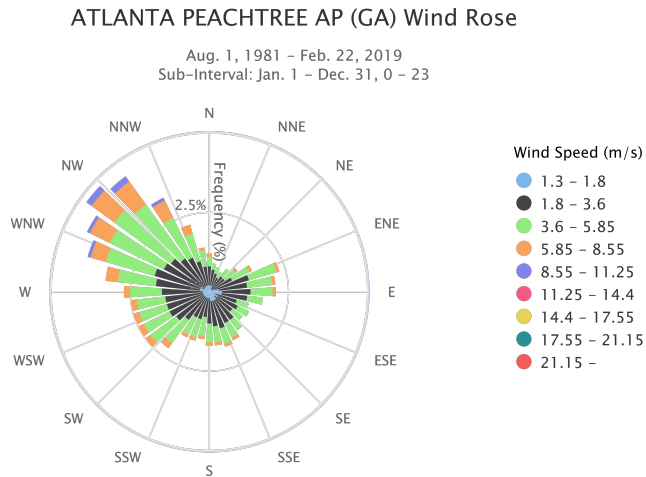

Figure 6: Wind rose of Atlanta Peachtree, Georgia, USA

3 Eurocode-Based Calculations

Throughout the calculations in this section, the structure is assumed to be fully rectangular. Also, the glass fins of the upper part are neglected. The corner cuttings (see figure 13b) are neglected. The simplified geometry is depicted in Figure 7.
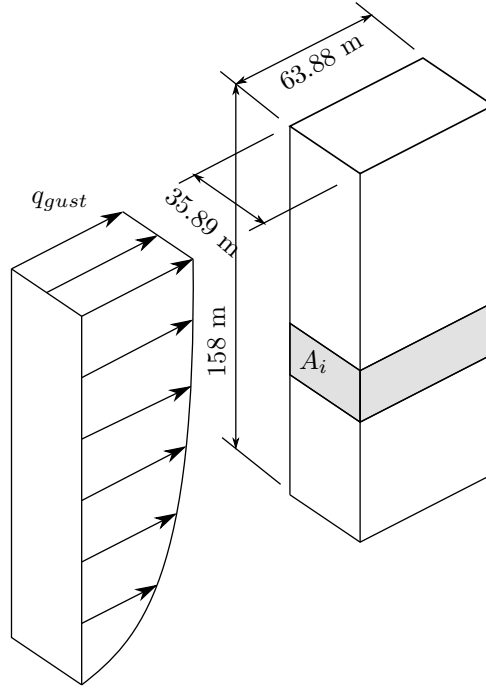
Figure 7: Simplified geometry for hand calculations (*first configurations*)

3.1 Aerostatic Responses

The pressure distribution based on a terrain category IV using the gust wind speed profile $u_{gust}(z)$ from (3) is assumed based on the Eurocode [11] as:

$$q_{gust}(z) = \frac{1}{2} \cdot \rho_{air} \cdot (u_{gust}(z))^2 \ , \tag{4}$$

where ρ_{air} is the density of the air, which is assumed to be 1.225 kg/m^3. Area slices are then formed on the buildings cross-wind section with a predefined slice height of h_i. The pressure distribution is assumed to be constant q_i upon the area of the slice $A_i = b \cdot h_i$, where b is the width of the building across wind direction. The static force on each slice is then calculated as:

$$F_i^{\text{static}} = q_i \cdot A_i \cdot c_f \ , \tag{5}$$

where c_f is the force coefficient. $c_f = 1.65,\ 2.3$ from Figure 8 (section 7.6 of Eurocode1 [11]), for the first and second configuration, respectively. The base shear and moment are then calculated as:

$$
\begin{aligned}
H &= \sum_i F_i \ , \\
M &= \sum_i F_i \cdot h_i \ .
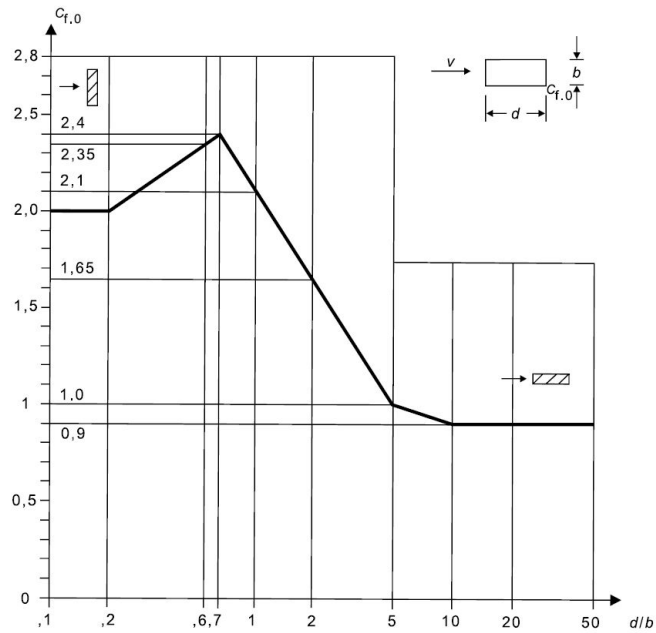\end{aligned}
\tag{6}
$$

Figure 8: Drag coefficient for sharp rectangular cross-section

The result of the calculations on our building are shown in figure 9. The base shear for the first and second configuration is 9.24 MN, and 25.83 MN, respectively. The base moment for the first and second configuration is 851.38 MNm, and 2380.96 MNm, respectively. This indicates that the *second configuration* is more critical, regarding base static shear and moment.

Table 1: Aeroelastic Static Responses

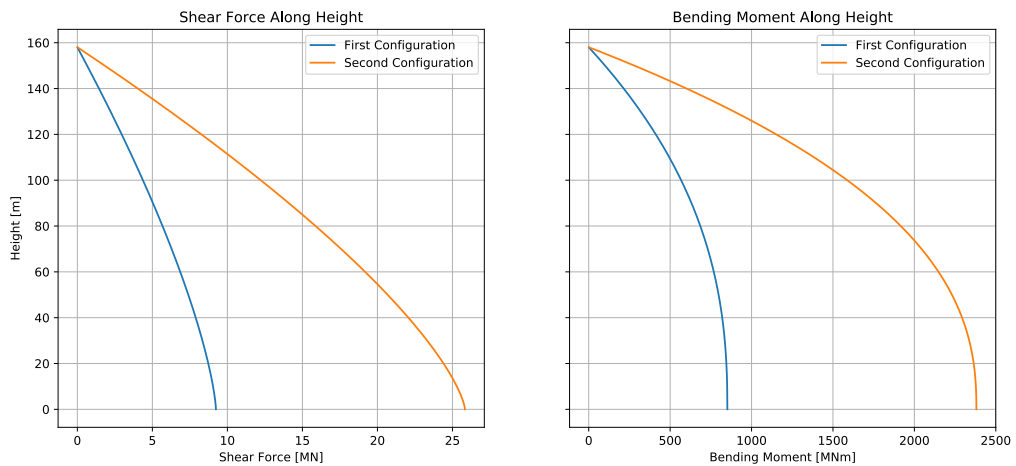| Configuration	Base Shear [MN]	Base Moment [MNm]
first	9.24	851.38
second	25.83	2380.96

Figure 9: Aeroelastic Forces Along Building's Height

3.2 Aerodynamic Responses

The aeroelastic dynamic response may be calculated as:

$$
\begin{aligned}
F_i^{\text{Dynamic}} &= c_s c_d \cdot c_f \cdot q_i \cdot A_i \\
&= c_s c_d \cdot F_i^{\text{static}} \ ,
\end{aligned}
\tag{7}
$$

where $c_s c_d$ is the structural factor [11], and F_i^{static} is calculated in (5). The structural factor $c_s c_d = 0.983, 0.9117$ for the *first* and *second* configurations, respectively. The calculation steps are in the appendix in section 6.1. Accordingly, the dynamic responses based on (7) are:

Table 2: Aeroelastic Dynamic Responses

configuration	Base Shear [MN]	Base Moment [MNm]
first	9.082	836.907
second	23.549	2170.721

3.3 Vortex Shedding

Vortex shedding is a phenomenon where the fluid flows over a bluff body, and vortices are shed in an alternating manner, which leads to a fluctuating load. To calculate the vortex shedding frequency and the critical velocity for vortex shedding, the Strouhal number, St, which is a dimensionless number for time-dependent specific oscillating flow, is used. It is defined as:

$$
St = \frac{fL}{u}
\tag{8}
$$

where f is the frequency, L is the characteristic length, and u is the characteristic velocity. The vortex shedding frequency then can be calculated using St obtained from Figure 10 (section E.1.3.2 of Eurocode1 [11]), the characteristic length defined as the width of the building across wind direction, and the characteristic velocity as the mean velocity v_b mentioned in (3). The shedding frequency is then for the *first configuration*:

$$
f^{(1)} = \frac{St_1 \cdot v_b}{L_1} = \frac{0.08 \cdot 28.27}{35.89} = 0.063 \text{ Hz} \ ,
\tag{9}
$$

and for the *second configuration*:

$$
f^{(2)} = \frac{St_2 \cdot v_b}{L_2} = \frac{0.12 \cdot 28.27}{63.88} = 0.053 \text{ Hz} \ .
\tag{10}
$$

The vortex shedding critical velocity is calculated via plugging in an approximation of the first eigenfrequency of the building as $n_1 = 46/h$ [11] into f in (8), obtaining for the *first configuration*:

$$
u_{crit}^{(1)} = \frac{46 \cdot L}{h \cdot St_1} = \frac{46 \cdot 35.89}{158 \cdot 0.08} = 130.61 \text{ m/s} \ ,
\tag{11}
$$

and for the *second configuration*:

$$
u_{crit}^{(2)} = \frac{46 \cdot L}{h \cdot St_2} = \frac{46 \cdot 63.88}{158 \cdot 0.12} = 154.98 \text{ m/s} \ .
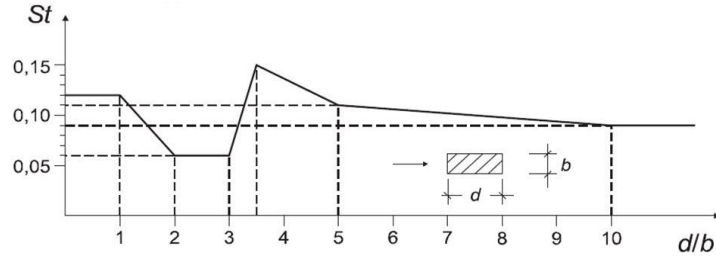\tag{12}
$$

Figure 10: Strouhal number for a sharp rectangular cross-section

.

According to E.1.2 from the Eurocode [11], the flow induced vibration phenomenon needs not to be considered when $u_{crit} > 1.25 \cdot u_b$. In the case of our building, $1.25 \cdot v_b = 35 < u_{crit}^{(1)}, \ u_{crit}^{(2)}$.

4 CFD-Based Calculations

4.1 Problem Setup

The wind tunnel dimensions of the CFD simulation are taken as in figure 11, where the height of our building, 1180 Peachtree, $h = 200 \ m$ [7].
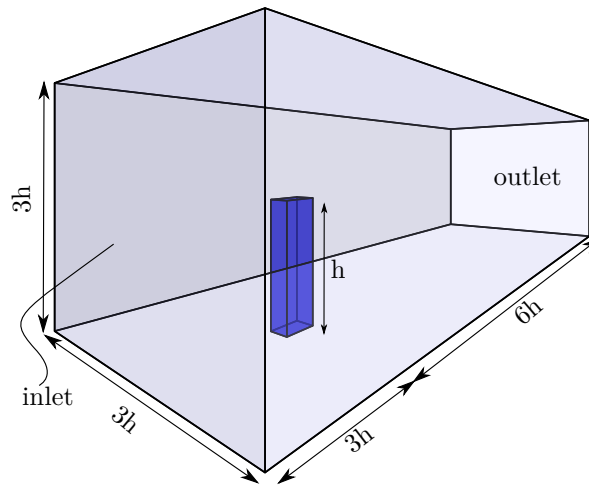

Figure 11: Bounding box dimensions

As mentioned before, the most critical wind directions are to be studied in this report. Mainly, two configurations are formed, namely, *first configuation* with a rotation angle defined as 0° depicted in Figure 12a, and a *second configuration* with a rotation angle of 90° depicted in Figure 12b. Also, the boundary conditions for inlet, outlet and outer walls are provided. In this study, a gust wind velocity profile is used as inlet boundary condition Outlet is modelled as outflow boundary and side walls and top wall have slip boundary condition. Ground (bottom wall) and building walls have no-slip boundary condition.
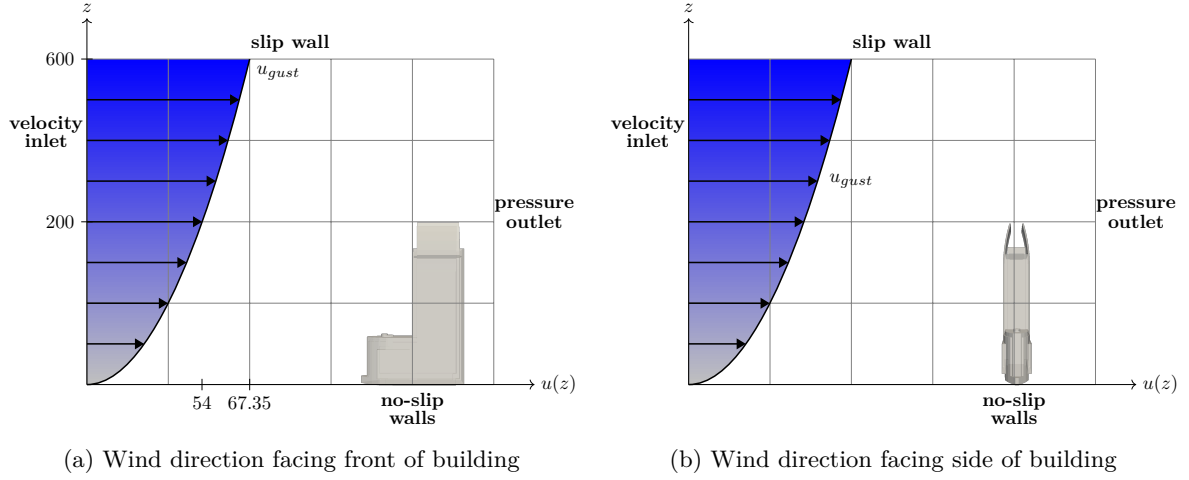
(a) Wind direction facing front of building   (b) Wind direction facing side of building

Figure 12: Boundary conditions for the problem setup.

4.2 Pre-Processing

Although having a well-detailed geometry could provide highly accurate results, this would also incur in a high computational cost due to the overhead generated due to the levels of refinement that the geometry would require. For such reason, some simplifications had to be done to avoid this scenario, while guaranteeing reliable results. These modifications are visible in figure 13. Some of these simplifications include the removal of the circular columns at the bottom of the building, increasing the thickness of the fins, and ignore other unnecessary features. These changes have no significance in our task. Regarding the gaps in the panels on top of the building, another setup in addition to the two main configuration is introduced without ignoring the gaps to study their effects on the vortex shedding and the pressure distribution.
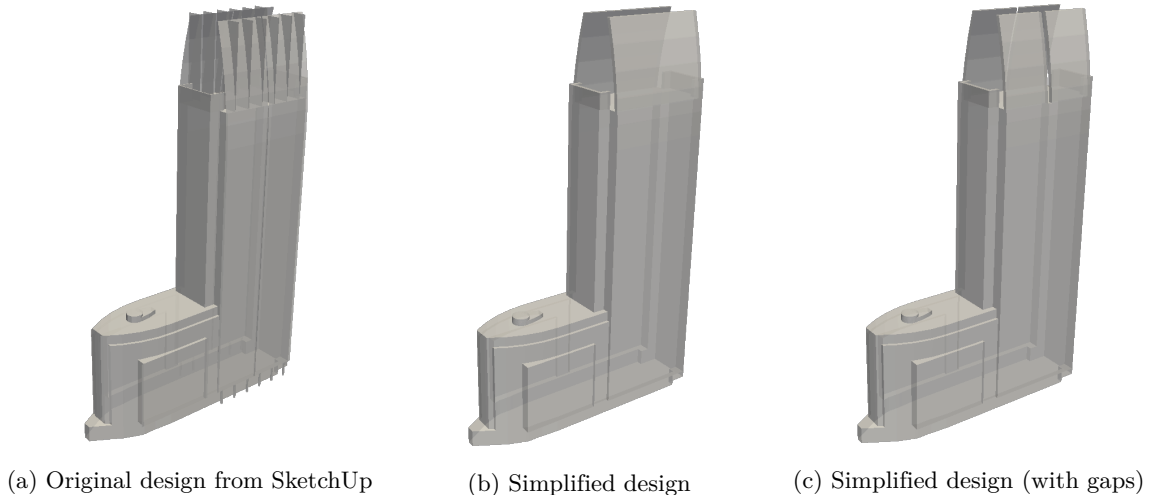

(a) Original design from SketchUp   (b) Simplified design   (c) Simplified design (with gaps)

Figure 13: 1180 Peachtree geometrical model

4.2.1 Meshing

In the *first configuration*, there are two refinement regions. The first (element size of 6 m) is to develop a velocity profile and capture the large eddies in the wake region behind the building, while the second region (element size of 1 m) is to capture the boundary layer on the surface of the building. The same

goes for the *second configuration* with slightly larger element sizes due to the fact that the building has a much wider length in y-direction in this configuration which increases the number of elements significantly. To solve this, the element sizes are increased and another refinement region is introduced. The sizes are depicted in Figure 14. The *first configuration* with the mesh size in Figure 14a yields $2,705,863$ elements, while the *second configuration* with and without introducing the gap in the panels yields $4,857,783$ and $3,789,924$ elements, respectively. The difference in the number of elements in between the building with and without the gap in the panels is because the first refinement zone in the former is extended more behind the building to better capture the eddies in the wake region, hence increasing the computational effort.

(a) First configuration
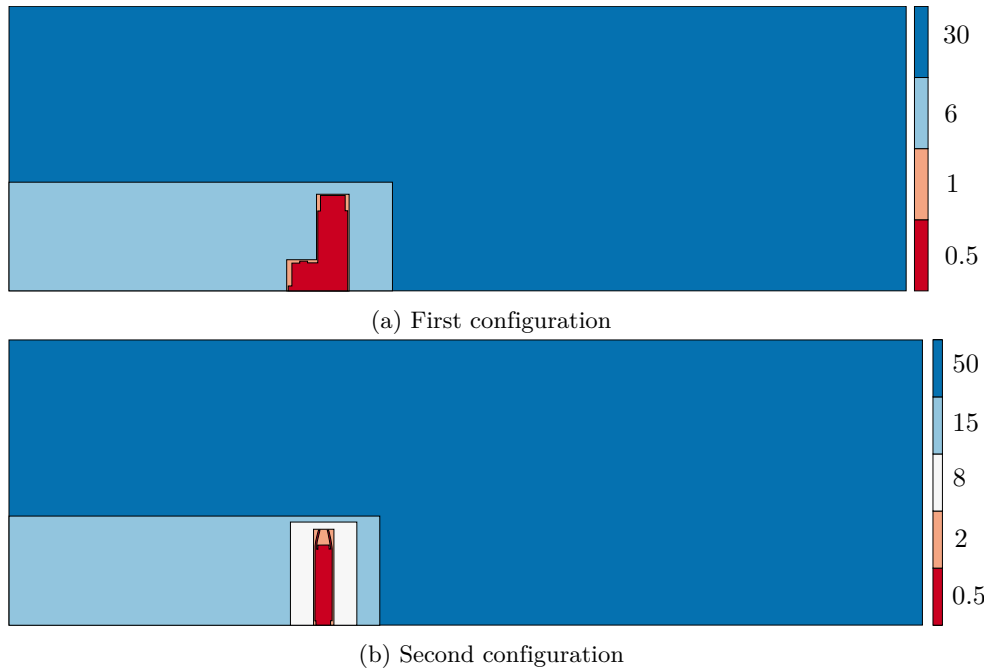

(b) Second configuration

Figure 14: Mesh sizes in the two configurations

The mesh was generated using the unstructured mesh generator in GiD [12] using the predefined mesh sizes as in figure 14. As an example, the mesh for the first simulation case is shown in figure 15.
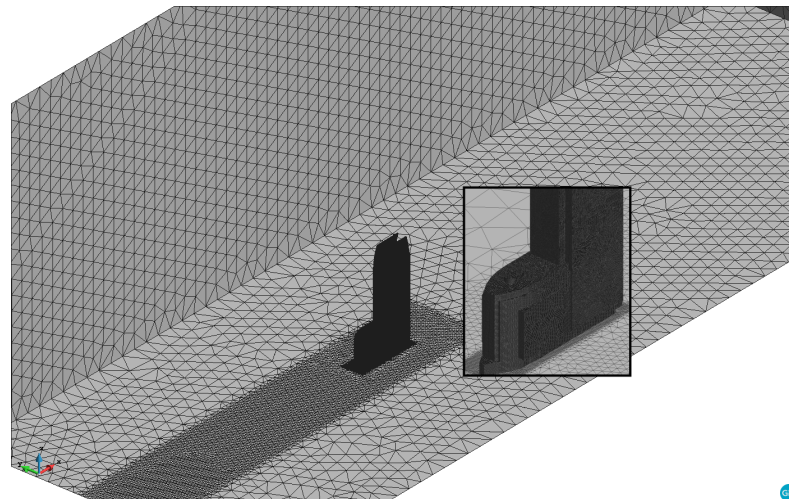

Figure 15: Mesh in the first configuration

The mesh is then, with the boundary conditions stated in section 4.1, simulated with KRATOS [5], using a turbulence model with finite elements [13].

4.2.2 Time Step

The time step should be chosen under two criteria, the CFL condition and the vortex shedding frequency. CFL (Courant – Friedrichs – Lewy) condition represents the ratio of the information traveling across an element and the size of the element in a mesh, which is defined in 1D as:

$$\text{CFL} = \frac{u \ \Delta t}{\Delta x} \ , \tag{13}$$

where u is the characteristic velocity, Δt is the time step size, and Δx is the mesh size. This ratio must be greater than one to guarantee stability of the solution. Using the smallest mesh size to obtain the worst CFL condition, in order to calculate the critical time step size:

$$\Delta t_{crit} = \frac{\Delta x \ \text{CFL}_{\text{crit}}}{u} = \frac{0.5 \cdot 1}{54} = 0.0093 \ s \ , \tag{14}$$

where u is the wind velocity on top of the building and CFL_{crit} is the critical CFL number, which should be ≤ 1 for explicit time integration schemes.

On the other hand, it is recommended to have at least 20-25 time steps per vortex shedding period. Using the vortex shedding frequencies in (9) and (10), the time period of vortex shedding is $\approx 15.87 \ s$ for the *first configuration* and $\approx 18.87 \ s$ for the *second configuration*. That indicates $\Delta t_{crit}^{(1)} \approx 0.635 \ s$ and $\Delta t_{crit}^{(2)} \approx 0.755 \ s$. It is clear that the CFL condition is dominating to select a time step. Since the time integration in Kratos is a fully implicit scheme [13] which allows for higher values in CFL number, the time step chosen to do the simulations is $\Delta t = 0.016 \ s$, which proved to be stable.

4.3 Results

In this section, the results from both analytical calculations based on the Eurocode [11] and the CFD simulation are presented. It is noteworthy to mention that for this kind of building with a large base and more slender top with an eccentricity, it is a common engineering practice to split the parts structurally. Therefore, this assumption is taken into account for calculating the drag forces and base aeroelastic reactions in the following. The simulation, however, takes into account the whole structure.

Here, the results of the three CFD simulations (first configuration and second configuration with and without the gaps) are shown. Paraview is used to perform the post-processing of the data.

4.3.1 Aeroelastic Dynamic Responses

The forces and moments with respect to the middle of the base of the tall part of the structure are shown in Figure 16. The simulation run time is 150 seconds. The first 20 seconds are highly oscillatory, so they are not considered here.

It is observed that the *first configuration* has a mean base shear (force in x-direction) of 6.82 MN and a mean base moment in y-direction (resulting from forces in x- and z-direction, while the z-direction forces are negligible due to the relatively small lever arm) of 712.6 MNm. The forces in y-direction are the vortex shedding forces and they have the same frequency of approximately 0.1 Hz. They have a higher contribution in the *first configuration* than in the *second*, because they are acting on the weak axis of the building. The forces in z-direction and the moments in z-direction (twisting moments) are relatively low.

On the other hand, in the *second configuration*, the force in x-direction is around 20.18 MN, and the moment in y-direction is around 1994.67 MNm. It is obvious that the *second configuration* is more critical in case of drag, but the vortex shedding forces and moments, and their periodicity is less dominant, due to the action on the strong axis of the building.
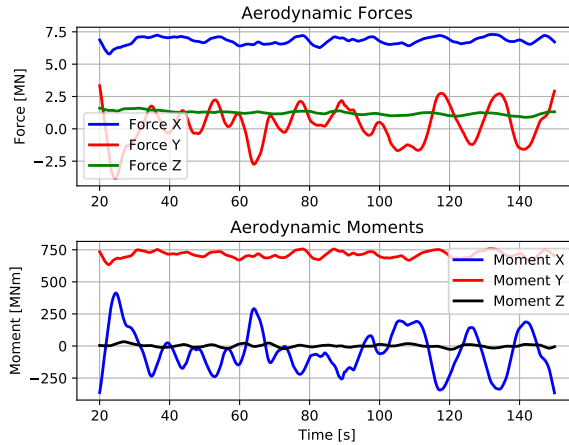
(a) First configuration
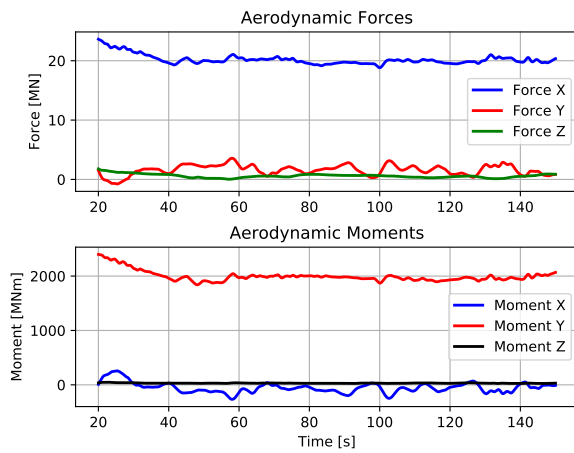
(b) Second configuration without Gaps
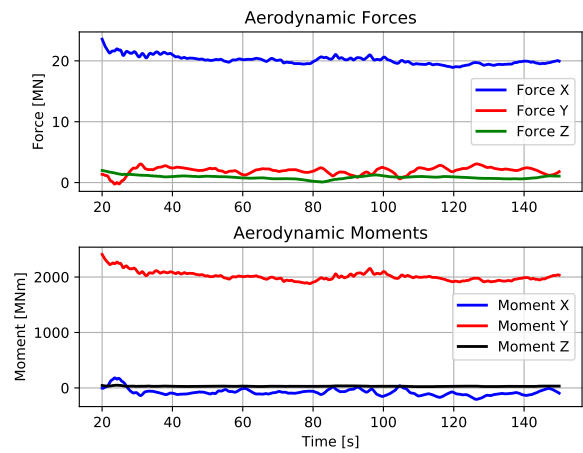
(c) Second configuration with Gaps

Figure 16: Aeroelastic forces and moments

4.3.2 Pressure distribution

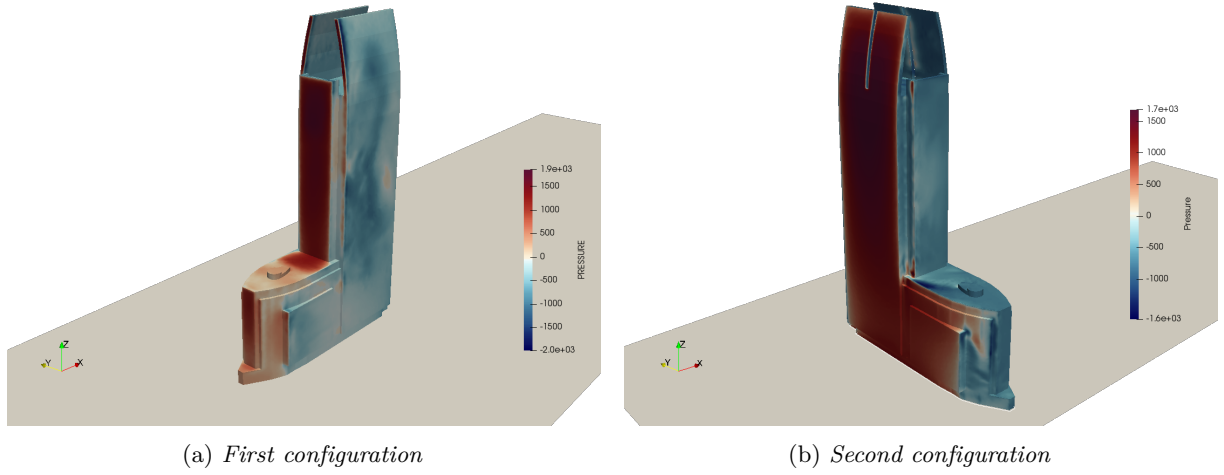(a) *First configuration*   (b) *Second configuration*

Figure 17: Pressure distribution over the surface of the building after 100 seconds

The pressure distribution on the surface area of the building at 100 seconds from the beginning of the simulation is shown in Figure 17. The high pressure values on the surface facing the flow is due to the stagnation point phenomenon, where the velocity reaches zero, which is at around two thirds the height of the building. It could be also observed in Figure 17a positive pressure values on the roof of the base structure due to the down-wash wind and the reattachment show in Figure 19. The down-wash wind phenomenon is usually important for engineering design at the pedestrian level, which is later explained in detail in section 4.3.5. The pressure on the sides of the buildings parallel to the flow is negative, which is interpreted as a suction pressure that is occurring after the wind flow has separated from the building surface at the sharp corner separating its face from its sides, creating a shear layer where negative pressure starts appearing at the building's side surfaces. One can notice that there is no reattachment of the wind on the sides of the building under such an extreme 50 years return period velocity field.

4.3.3 Cp values

Iso-contours of the Cp values, at 100 seconds from the beginning of the simulation, on different sides of the building are shown in Figure 18. These results can be helpful to understand the concept behind pressure coefficient values given in wind loading standards. The maximum normalized pressure coefficient Cp value on the windward side of the building obtained from the simulations is 1.3 and 1.1 for the *first* and *second* configurations, respectively. Maximum negative value is $\approx$ -1.5 for both first and second configurations (located at the back of the building and at the base of the building, where the maximum suction pressure occurs).
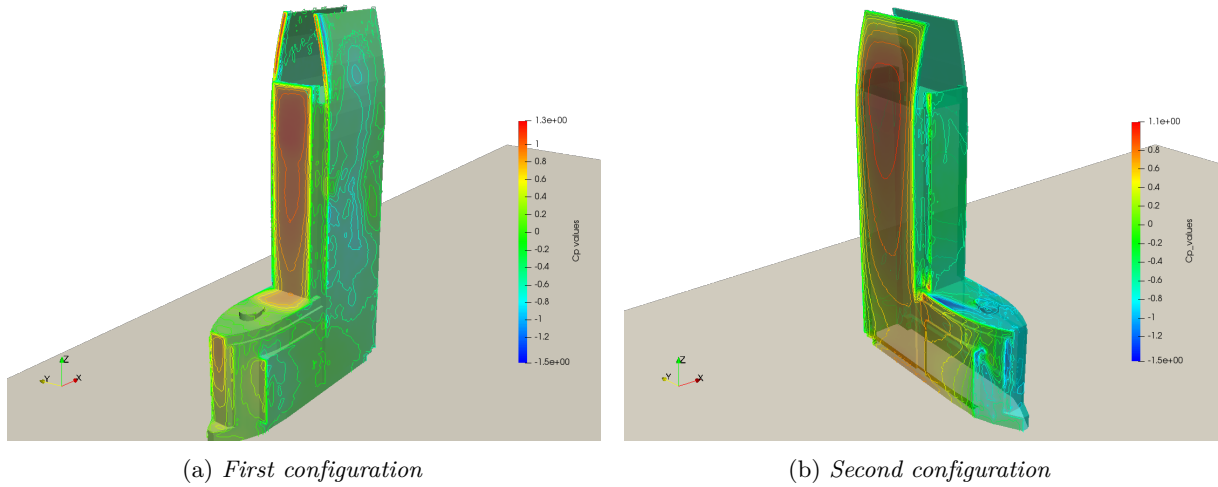
(a) *First configuration*   (b) *Second configuration*

Figure 18: Iso-contours of the Cp values over the surface of the building after 100 seconds

4.3.4 Velocity field

Figures 19 to 22 show the velocity field at different sections of the fluid domain and different heights of the building. It is clearly seen the stream line deviation at sharp corners of the building and wake structure generation at leeward (downwind) side of the building.

Figure 19 shows the velocity field of the *first configuration* at 100 seconds. The flow passes in between the fins and recirculates behind the building forming the vortices with noticeably lower velocity values. Comparing the *first configuration* in Figure 19 with the *second configuration* in Figure 20, one could notice the difference in size of the wake region. This is mainly caused by the larger across-wind area of the bluff body obstructing the wind stream. In addition, comparing the models with and without gaps (Figures 20a and 20b), the wake region is different due to the fact that the gap allows wind flow inside instead of traveling to the edges of the fins. The wake region is then slightly smaller. The flow inside the gaps however has a high velocity due to the small opening (Venturi effect). This is shown as well in Figure 22.

It should be noted that in this project, due to mesh restrictions, an overestimation of the gap had to be made in order to have a better quality mesh. In the real case with a narrower opening, the impact of the gap on the wake would be less to a certain degree but the velocity inside would be higher.
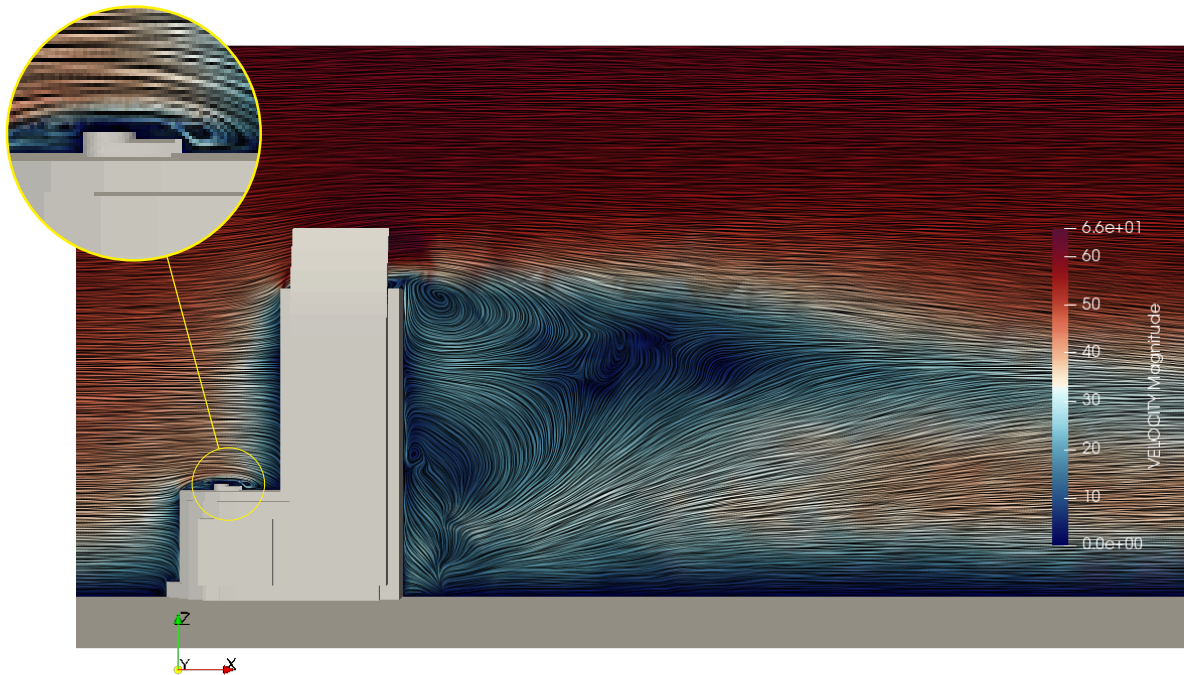
Figure 19: Velocity field for the *first configuration* after 100 seconds. Clip over the XZ plane
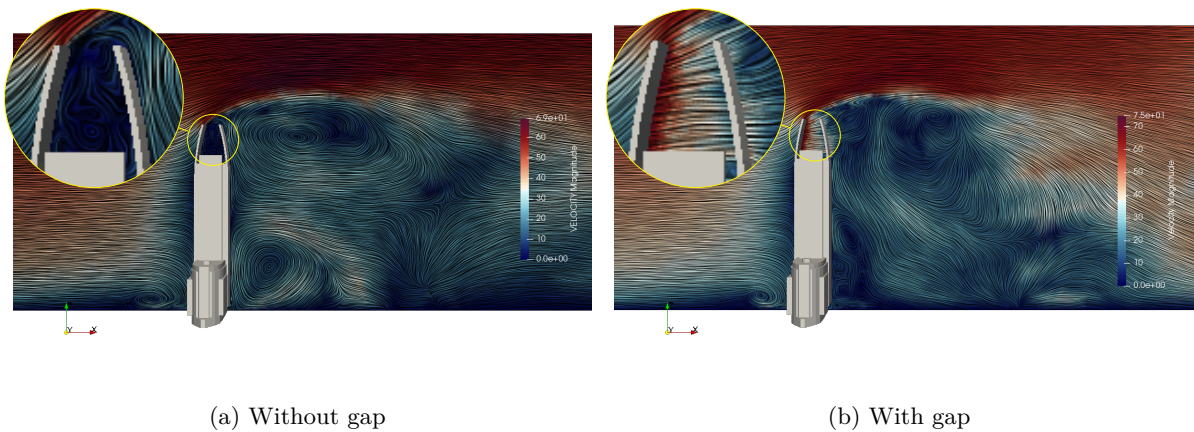
(a) Without gap

(b) With gap

Figure 20: Velocity field for the *second configuration* after 100 seconds. Clip over the XZ plane

Figure 21 shows two types of vortex patterns in the wake of the building for both configurations at the height of $\frac{2}{3}h$. In Figure 21a there is a near vortex formation due to strong roll-up of separated shear layers, while in Figure 21b there is far vortex formation due to weak roll-up of separated shear layers.
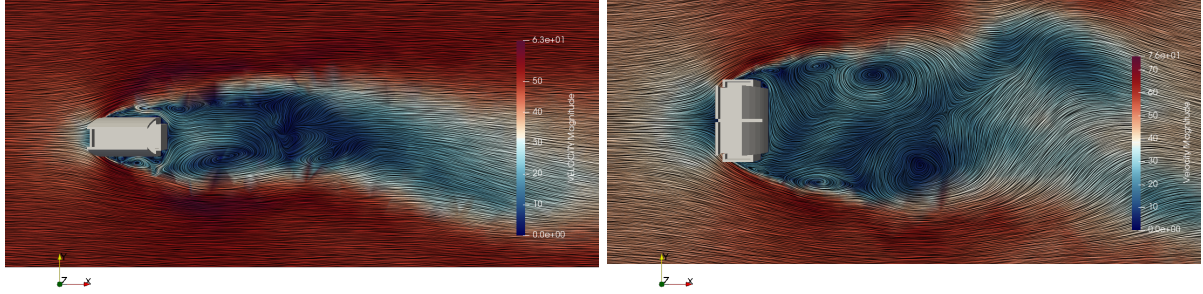
(a) *First configuration*   (b) *Second configuration*
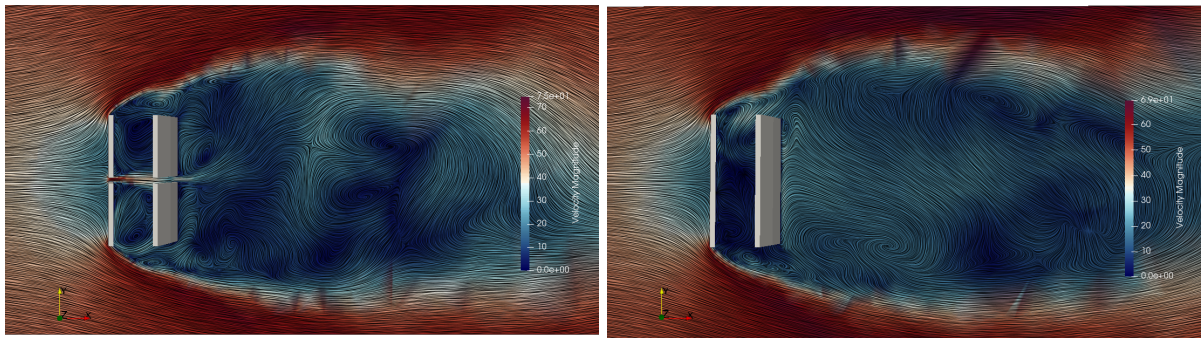
Figure 21: Velocity field at a height of $2/3 \cdot h$ after 100 seconds

(a) Velocity field at $9/10 \cdot h$. With gap   (b) Velocity field at $9/10 \cdot h$. Without gap

Figure 22: Velocity field for *second configuration* at $9/10 \cdot$ h after 100 seconds

4.3.5   Wind comfort

Additional to the structural and aeroelastic response of the building, a basic wind comfort assessment can be performed by inspecting the wind velocity at pedestrian level. Figure 23 shows the wind velocity around the building, for both configurations, at 1.75 m from ground level (approximately the average height of male population in the USA). It is seen that the maximum velocity present in the *first configuration* (Figure 23a) is ~40 m s^{-1}, while in the *second configuration* is ~62 m s^{-1}, located at the corners of the building. There are several factors involved which cause the velocity values to be extremely high and uncomfortable, not to mention alarming, according to the comfort velocity of 5 m s^{-1} proposed in [14]. The deprecation of the columns visible in Figure 13a, which serve as wind dissipators, and the fact that no other building surrounding the structure was included in the simulation (the wind directly impacts the building without any obstacle) are two of the main sources of these discrepancies.

Although these values are out of proportion, they provide an insight on where to take precautions at the time of designing a building.
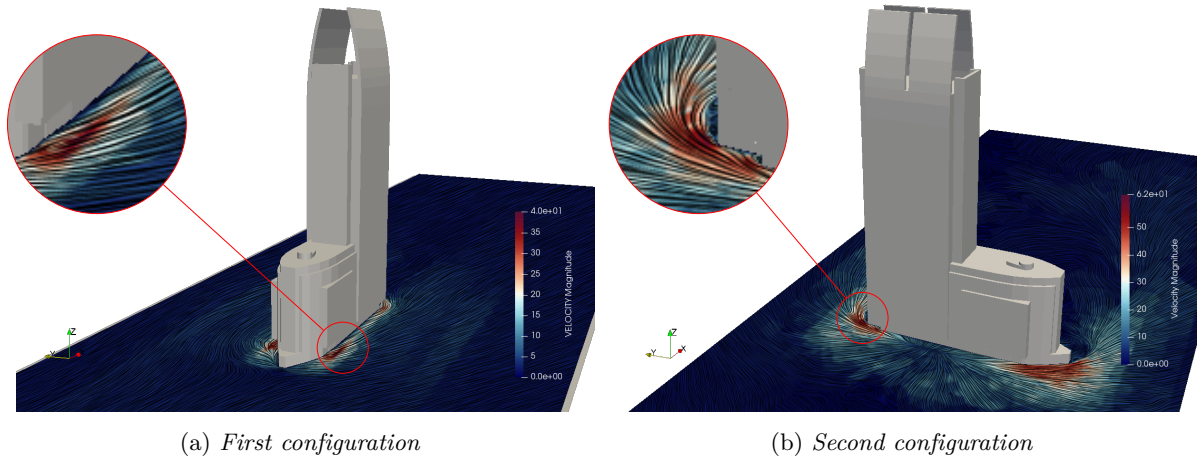
(a) *First configuration*   (b) *Second configuration*

Figure 23: Velocity field at a height of 1.75 m from ground level

5 Validation of the Simulation

In this section, the results of the Eurocode based calculations in section 3 and and CFD results in section 4.3 are compared.

5.1 Aeroelastic Response

The aeroelastic responses are shown in the following table:

Table 3: Comparison of the aeroelastic response

Configuration	Static Base Shear [MN]	Dynamic Base Shear [MN]	CFD Base Shear [MN]	Static Base Moment [MNm]	Dynamic Base Moment [MNm]	CFD Base Moment [MNm]
first	9.24	9.082	6.82	851.38	836.907	712.6
second	25.83	23.549	20.18	2380.96	2170.721	1994.67

The relative error between the static calculations and the CFD results averages on 25.58%, and between the dynamic calculations and CFD results 19.03%. This error may indicate the factor of safety in the Eurocode calculations. One can notice that the dynamic results produce less forces than the static results which leads to a more optimized design.

5.2 Vortex Shedding

The frequencies of the vortex shedding is shown in the following table:

Table 4: Comparison of the vortex shedding frequency

Configuration	analytical	CFD
first	0.063	0.085
second	0.053	0.069

The CFD vortex shedding frequency is estimated based on Figure 16. The relative error average is -24.53%. Strouhal number can then be obtained based on (8) for the CFD results to be compared with the analytical, which leads to:

Table 5: Comparison of Strouhal number

Configuration	analytical	CFD
first	0.08	0.1079
second	0.12	0.1559

Conclusion and Outlook

A structural wind analysis has been established on the high-rise building 1180 Peachtree in Atlantna, Georgia, United States, by two means, analytically using the Eurocode1 and computationally using CFD wind tunnel simulations.

First, wind data was obtained from a nearby station as a daily maxima for the last eight years. The data was used to establish a wind velocity and pressure profiles. The profiles are applied on orientations of the building to study the most critical configuration yielding two main configurations.

Second, relatively large simplifications were assumed to carry on calculations based on Eurocode1. The aeroelastic static as well as the dynamic responses are calculated and presented, leading to a deduction that the *second configuration* being more critical. Also, the vortex shedding frequencies and velocities are estimated.

Third, relatively less simplifications were made yielding three wind tunnel simulation. One in the *first configuration*, and two in the *second configuration* with and without gaps in the top fins. The aeroelastic responses are also calculated and the vortex shedding frequencies are estimated. The results of the pressure distribution, pressure coefficients, and velocity fields are presented. It is denoted that the configurations produce different wind flows in the wake region, and the gap has a noticable effect on the wind flow. The pedestrian wind comfort was also studied to highlight the critical areas where the wind flow is the highest around the building.

Finally, the simulations are validated by comparing the analytical to the computational calculations. The average relative error in the results is 21.78%.

The effects of Flow Induced Vibrations (FIV), such as galloping, which normally requires Fluid-Structure Interaction (FSI) simulations are not considered in this report, due to its complexity of solving the fluid domain and the dynamic structural domain and couple the results. Also, finer meshes could be established in order to guarantee a mesh-independent better solution. Additionally, less simplifications in the analytical solution would lead to more accurate results.

To conclude, the behavior of the building against wind has been analyzed. The results of the wind impact on the building is shown as well as the building's impact on the down-wind. The effect of the gaps in the fins also proved to have a slight change in the wake region but does not noticeably affect the forces and moments exerted on the building. Some modifications could be done to enhance pedestrian comfort around the building.

REFERENCES

[1] AU Weerasuriya and MTR Jayasinghe.
"Wind loads on high-rise buildings by using five major international wind codes and standards".
In: *Engineer* 47.03 (2014), pp. 13–25.

[2] Tetsuro Tamura.
"Reliability on CFD estimation for wind-structure interaction problems".
In: *Journal of Wind Engineering and Industrial Aerodynamics* 81.1-3 (1999), pp. 117–143.

[3] AD Gosman.
"Developments in CFD for industrial and environmental applications in wind engineering".
In: *Journal of Wind Engineering and Industrial Aerodynamics* 81.1-3 (1999), pp. 21–39.

[4] Theodore Stathopoulos.
"Computational wind engineering: Past achievements and future challenges".
In: *Journal of Wind Engineering and Industrial Aerodynamics* 67 (1997), pp. 509–532.

[5] KRATOS.
URL: http://www.cimne.com/kratos/.

[6] *1180 Peachtree - Atlanta - Properties - Hines.*
URL: https://www.hines.com/properties/1180-peachtree-atlanta.

[7] Heinz H. Hansen and Clayton Odom.
1180 Peachtree.
URL: https://www.emporis.com/buildings/183231/1180-peachtree-atlanta-ga-usa.

[8] *1180 Peachtree.*
URL: https://3dwarehouse.sketchup.com/model/c9bcc78ccdf7e6b57c7fe35036d999cf/1180-Peachtree?hl=en.

[9] Mihir Zaveri, Guilbert Gates, and Karen Zraick.
The Government Shutdown Was the Longest Ever. Here's the History.
Jan. 2019.
URL: https://www.nytimes.com/interactive/2019/01/09/us/politics/longest-government-shutdown.html.

[10] National Centers for Environmental Information and Ncei.
Climate Data Online.
URL: https://www.ncdc.noaa.gov/cdo-web/.

[11] *EN 1991-1-4 Eurocode 1: Actions on structures - Part 1-4: General actions - Wind actions.*
EN. Brussels: CEN, 2005.

[12] *GiD - The personal pre and post processor.*
URL: https://www.gidhome.com/.

[13] Jordi Cotela Dalmau.
"Applications of turbulence modelling in civil engineering".
PhD thesis. Jan. 2016.
DOI: 10.13140/RG.2.1.3510.1845.

[14]   Bert Blocken, WD Janssen, and Twan van Hooff.
       "CFD simulation for pedestrian wind comfort and wind safety in urban areas: General decision
       framework and case study for the Eindhoven University campus".
       In: *Environmental Modelling & Software* 30 (2012), pp. 15–34.

[15]   Sanaul Huq. Chowdhury.
       "Damping characteristics of reinforced and partially prestressed concrete beams".
       PhD thesis. 1999.

6 Appendix

6.1 Calculation of The Structural Factor $c_s c_d$

$$c_s c_d = \frac{1 + 2 \cdot k_p \cdot l_v(z_s) \cdot \sqrt{B^2 + R^2}}{1 + 7 \cdot l_v(z_s)} \ , \tag{15}$$

where z_s is the reference height, k_p is the peak factor, $l_v(z)$ is the turbulence intensity, B^2 is the background factor, R^2 is the resonance response factor [11]. The structural factor is decomposed into c_s and c_d, which are the size and the dynamic factors, respectively.

For our building, the reference height is taken as: $z_s = 0.6 \cdot h = 0.6 \cdot 158 = 94.8 \ m$. The turbulence intensity is:

$$\begin{aligned} l_v(z_s) &= \frac{1}{c_o(z_s) \cdot \ln\left(\frac{z_s}{z_0}\right)} \\ &= \frac{1}{\ln(94.8)} = 0.2197 \ , \end{aligned} \tag{16}$$

where the orography factor $c_o = 1$ for a flat ground, and the roughness length $z_0 = 1$ for a terrain category IV (table 4.1 of [11]). The background factor is:

$$B^2 = \frac{1}{1 + 0.9 \cdot \left(\frac{b+h}{L(z_s)}\right)^{0.63}} \ , \tag{17}$$

where the turbulence length scale at the reference height $L(z_s)$ is:

$$L(z_s) = L_t \cdot \left(\frac{z_s}{z_t}\right)^{0.67 + 0.05 \ln(z_0)} = 300 \cdot \left(\frac{94.8}{200}\right)^{0.67} = 181.925 \ , \tag{18}$$

where $L_t = 300 \ m$ is a reference height scale and $z_t = 200 \ m$ is a reference height section B.1 in Eurocode1 [11]). The background factor is then 0.51, 0.4767 for the *first* and *second* configurations, respectively. The resonance response factor is:

$$R^2 = \frac{\pi^2}{2 \cdot \delta} \cdot S_L(z_s, n_1) \cdot R_h(\eta_h) \cdot R_b(\eta_b) \ , \tag{19}$$

where the logarithmic decrement damping δ is assumed to be 0.035 for concrete structures [15]. The non-dimensional power spectral density function is:

$$S_L(z_s, n_1) = \frac{6.8 \cdot f_L(z_s, n_1)}{(1 + 10.2 \cdot f_L(z_s, n_1))^{5/3}} = 0.0905 \ , \tag{20}$$

where the non-dimensional frequency f_L is:

$$f_L(z_s, n_1) = \frac{n_1 \cdot L(z_s)}{u_{mean}(z_s)} = \frac{0.2911 \cdot 181.925}{31.095} = 1.703 \ , \tag{21}$$

where $n_1 = 46/h = 46/158 = 0.2911$ is an approximation to the first eigenfrequency of the building and $u_{mean}(z_s) = 0.56 \cdot (39.59/1.4) \cdot (94.8/10)^{0.3}$ is calculated using (3). Then, the aerodynamic admittance functions are:

$$\begin{aligned} R_h &= \frac{1}{\eta_h} - \frac{1}{2\eta_h^2} \cdot \left(1 - e^{-2\eta_h}\right) \\ R_b &= \frac{1}{\eta_b} - \frac{1}{2\eta_b^2} \cdot \left(1 - e^{-2\eta_b}\right) \ , \end{aligned} \tag{22}$$

where $\eta_h = 4.6 \cdot h/L(z_s) \cdot f_L(z_s, n_1) = 6.804$ and $\eta_b = 4.6 \cdot b/L(z_s) \cdot f_L(z_s, n_1) = 1.5456, \ 2.75$, for the *first* and *second* configurations, respectively. Then,

$$R_h = 0.136, \quad R_b^{(1)} = 0.4472, \quad R_b^{(2)} = 0.2978 \ . \tag{23}$$

Plugging the values from (20) and (23) into (19), we get:

$$
\begin{aligned}
R_{(1)}^2 &= \frac{\pi^2}{2 \cdot 0.035} \cdot 0.0905 \cdot 0.136 \cdot 0.4472 = 0.776 \ , \\
R_{(2)}^2 &= \frac{\pi^2}{2 \cdot 0.035} \cdot 0.0905 \cdot 0.136 \cdot 0.2978 = 0.5168 \ .
\end{aligned}
\tag{24}
$$

The only part left from (15) is now the peak factor which is:

$$k_p = \sqrt{2 \cdot \ln(\nu T)} + \frac{0.6}{\sqrt{2 \cdot \ln(\nu T)}} \ , \tag{25}$$

where $\nu = n_1 \cdot \sqrt{R^2/(B^2 + R^2)} = 0.2261, \ 0.2065$ for the *first* and *second* configurations, respectively, and the average time for the mean wind velocity $T = 600 \ s$. Given that, $k_p^{(1)} = 3 = k_p^{(2)}$ because the maximum value of k_p is 3.

Finally, Plugging in the calculated values into (15), the structural factor is then,

$$
\begin{aligned}
c_s c_d^{(1)} &= \frac{1 + 2 \cdot 3 \cdot 0.2197 \cdot \sqrt{0.51 + 0.776}}{1 + 7 \cdot 0.2197} = 0.983 \\
c_s c_d^{(2)} &= \frac{1 + 2 \cdot 3 \cdot 0.2197 \cdot \sqrt{0.4767 + 0.5168}}{1 + 7 \cdot 0.2197} = 0.9117
\end{aligned}
\tag{26}
$$